This is the peer-reviewed, final accepted version for American Mineralogist, published by the Mineralogical Society of America.
The published version is subject to change. Cite as Authors (Year) Title. American Mineralogist, in press.
DOI: https://doi.org/10.2138/am-2022-8207. http://www.minsocam.org/

Word Count: 5247

Revision 1

# Evaluating the physicochemical conditions for gold occurrences in pyrite

**Hongping He[1,2,3*], Haiyang Xian[1,2], Jianxi Zhu[1,2], Wei Tan[1,2], Xiao Wu[1,2,3], Yiping Yang[1,2], Shan Li[1,2], Kunfeng Qiu[4], Runliang Zhu[1,2], and H. Henry Teng[5]**

[1] *CAS Key Laboratory of Mineralogy and Metallogeny/Guangdong Provincial Key Laboratory of Mineral Physics and Materials, Guangzhou Institute of Geochemistry, Chinese Academy of Sciences (CAS), Guangzhou 510640, China.*

[2] *CAS Center for Excellence in Deep Earth Science, Guangzhou, 510640, China*

[3] *University of Chinese Academy of Sciences, Beijing 100049, China.*

[4] *State Key Laboratory of Geological Processes and Mineral Resources, School of Earth Sciences and Resources, China University of Geosciences, Beijing 100083, China*

[5] *Institute of Surface-Earth System Science, Tianjin University, Tianjin 300072, China*

*Correspondence to: H. P. He (hehp@gig.ac.cn).

## Abstract

While noble metals often occur as minor components in host minerals in various ore deposits, little theoretical assessment exists to predict the occurrence of these metals. Here, we probe the fundamental controls responsible for the occurrence of trace elements in host minerals through first-principles calculations. We apply the theoretical model to understanding the debated issues concerning the occurrence of gold (Au) in pyrite, in which the valence of Au is ascribed to either

positive or negative values. Our results indicate that (1) both positive and negative valent Au may occur in pyrite and (2) higher sulfur fugacity and lower temperature lead to more $Au^{+}$ occupying Fe sites in pyrite. These findings suggest that chemical states and speciation of the Au in host pyrite are ultimately controlled by temperature and sulfur fugacity, providing insight into the formation conditions of ore deposits and facilitating strategy design for beneficiation.

**Keywords:** gold-bearing pyrite, physicochemical condition dependence, gold occurrence, density functional theory, thermodynamics, sulfur fugacity

## Introduction

Gold (Au) not only is of great importance for financial reserves but also, like other trace elements including indium, germanium, and tellurium, etc., is required in unprecedented quantities in industrial applications (Gulley et al. 2018). Due to low abundance (parts to sub-parts per million), Au, as well as other trace elements, frequently disperse in host minerals as solute constituents of solid solutions (Zhai et al. 2019). The physicochemical state and speciation that these metals assume in the corresponding hosts often carry critical information indicative of the ore formation processes (Xing et al. 2019; Du et al. 2020), in addition to being a key gauge for downstream metal recovery (Wang et al. 2008). Despite such general understanding, strategies rationalizing the occurrence of noble metals in host minerals remain largely empirical. The lack of a theoretical basis to investigate the occurrence of valuable metals impedes the interpretation of genetic information of metallogenic processes and high-efficient recovery of these metals.

Pyrite ($FeS_2$) occurs in almost all metalliferous deposits and is a predominant gold-bearing

mineral in many giant gold deposits such as the Carlin-type (Reich et al. 2005). Although the occurrence of Au in pyrite has been of wide concern, the chemical state and site occupation of Au are still in debate. Previous studies, based on spectroscopy (Li et al. 1995; Simon et al. 1999; Cabri et al. 2000; Trigub et al. 2017; Merkulova et al. 2019; Pokrovski et al. 2019) or charge balance consideration (Chouinard et al. 2005), focused primarily on samples from specific deposits while ignoring the substitutional physics of pyrite and the physicochemical conditions under which it formed. This results in a historical paradox of the oxidation state of Au in pyrite, i.e., either positive or negative oxidation state. The positive +1 and +3 valences are interpreted from X-ray absorption near edge structure (XANES) spectroscopy and charge balance consideration (Simon et al. 1999; Cabri et al. 2000; Trigub et al. 2017; Merkulova et al. 2019; Pokrovski et al. 2019), while the negative oxidation state of gold is confirmed by X-ray photoelectron spectroscopy (XPS) and Mössbauer spectroscopy (Li et al. 1995, 2002). Therefore, we hypothesize that the inconsistency of the interpretation of gold occurrence in pyrite may be caused by variations of site occupations and formation conditions.

Herein, we propose a theoretical framework, which links the occurrence of Au in pyrite structure to its metallogenic environments, to test the hypothesis. For a host mineral, the incorporated elements are *de facto* impurities whose site occupancy in host minerals can be treated as a distribution of the impurity elements in a crystal field, which can be described by the Maxwell-Boltzmann distribution. In such a system, the occupation probability of the impurity elements at different lattice sites of host minerals hinges upon both the incorporation-energy-level and the temperature. The incorporation energy of impurity elements into a host mineral is commonly controlled by the chemical potential of the

elements in the host lattice, which in turn is related to the environments where the host crystals grew. Hence, the occupation probability and electron structure of metals in their host minerals can be precisely assessed, with the employment of modern first-principles techniques, under various growth environments.

We quantify the probability of Au occurrence in pyrite by evaluating the Boltzmann factor governing the atomic distribution in the lattice of the host mineral. The Boltzmann factor ($w$) is defined as:

$$w = \frac{p_i}{p_0} = e^{\frac{-\varepsilon_i}{kT}}, \qquad (1)$$

where $p_0$ and $p_i$ denote the probabilities of Au occurrence locating at the first (i.e., the ground state) and $i^{\text{th}}$ incorporation-energy-level ($\varepsilon_i$), respectively; $k$ and $T$ are the Boltzmann constant and temperature, respectively. The sum of the occurrence probabilities, $p_i$, equals to 1, i.e.,

$$\Sigma p_i = 1. \qquad (2)$$

By relating the occurrence probability to the corresponding electronic structure, we find that the stability field can be associated with either positive or negative valence state in a wide range of physicochemical environments, suggesting the site occupation and valence state of Au in pyrite can serve as a genetic proxy for the formation of pyritic Au deposits.

## Methods

### Density functional theory calculations

The density functional theory (DFT) calculations were performed using the Vienna Ab initio Simulation Package (VASP.5.4.4) (Kresse and Furthmuller 1996) along with the projector augmented

wave (PAW) method (Kresse and Joubert 1999). Standard PAW pseudopotentials (Fe: $d^7s^1$, S: $s^2p^4$, Au: $s^1d^{10}$, and Cs: $5s^5p^6s$) were used. The generalized gradient approximation (GGA) formulation by Perdew, Burke, and Enzerhoff (PBE) functional (Perdew et al. 1996) was used to describe the exchange-correlation interaction among electrons, and the energy of 400 eV was used as a cutoff value for the plane wave basis. Total energies were converged at $10^{-6}$ eV. The simplified Hubbard *U* correction (GGA+*U*) method (Dudarev et al. 1998) was employed to describe the 3*d* electrons of Fe element. The parameter *U*-*J*= 1.6 eV was employed, and the feasibility of such a parameter was confirmed by previous studies on pyritic systems (Zhang et al. 2012; Xian et al. 2019b, 2019a, 2021). The calculated lattice constant of 5.423 Å is in good agreement with both the experimental data and previous calculations (Table 1). All the structures employed in this study were relaxed until forces became smaller than 0.02 eV/Å. The ab initio molecular dynamics (AIMD) calculations were performed in NVT ensemble with Nosé-Hoover chain thermostats (Martyna et al. 1992) under 298 K. The time step of the AIMD runs was 1 fs. The visualization and analyses of the AIMD trajectories were performed by the package of VASPKIT (Wang et al. 2021) and VMD (Humphrey et al. 1996). The theoretical valence state was treated by the Bader charge-division scheme based on the electronic charge density (Bader 1990), which was embedded in the code developed by the Henkelman Group (Henkelman et al. 2006; Tang et al. 2009). The qualitative oxidation state of Au can be identified from the Bader charge, although the Bader charge cannot directly represent the chemical oxidation state.

The pyrites with Au located at various sites were modeled by 2 × 2 × 2 supercells with 96 (for the substitution cases) or 97 (for the interstitial incorporation model) atoms. For the interstitial model,

This is the peer-reviewed, final accepted version for American Mineralogist, published by the Mineralogical Society of America.
The published version is subject to change. Cite as Authors (Year) Title. American Mineralogist, in press.
DOI: https://doi.org/10.2138/am-2022-8207. http://www.minsocam.org/

the site was randomly selected from an interstitial site in the pyrite structure, as all the interstitial sites are symmetrically equivalent. The configuration files of reference materials (including AuS, CsAu, and elemental Au, Fe, and S) were downloaded from the Materials Project website (Jain et al. 2013). Structure relaxation of these configurations was modeled by the unit cells. The calculated lattice parameters of the reference materials are in good agreement with experimental or previous calculated values (Table 1).

**Calculations of the incorporation-energy-level and the occurrence probability**

The Au incorporation energies ($E_i$) in these pyritic models were calculated through the equation:

$$E_i = E_{gpy} - E_g - E_{py} + \mu_{atom}^{sub}, \qquad (3)$$

where $E_{gpy}$, $E_g$, and $E_{py}$ denote the DFT total energies of the gold-bearing pyrite, one Au atom in gold metal, and the pure pyrite, respectively. $\mu_{atom}^{sub}$ denotes the chemical potential of specific substitutional atom (i.e., the chemical potential of Fe ($\mu_{\mathrm{Fe}}^{\mathrm{py}}$) and S ($\mu_{\mathrm{S}}^{\mathrm{py}}$) of pyrite in this study). Mathematically, $\mu_{\mathrm{Fe}}^{\mathrm{py}}$ and $\mu_{\mathrm{S}}^{\mathrm{py}}$ obey the constraint

$$\mu_{\mathrm{Fe}}^{\mathrm{py}} + 2\mu_{\mathrm{S}}^{\mathrm{py}} = \mu_{\mathrm{FeS_2}}^{\mathrm{py}}, \qquad (4)$$

where $\mu_{\mathrm{FeS_2}}^{\mathrm{py}}$ denotes the chemical potential of one $FeS_2$ formula unit in pyrite. For simulations relevant to various sulfur environments, $\mu_{\mathrm{S}}^{\mathrm{py}}$ refers to the alpha S elementary crystal phase (α-S). Thus, the sulfur environments were characterized by the chemical potential difference, $\Delta\mu_{\mathrm{S}}$.

$$\Delta\mu_{\mathrm{S}} = \mu_{\mathrm{S}}^{\mathrm{py}} - \mu_{\mathrm{S}}^{\alpha-\mathrm{S}}. \qquad (5)$$

The relative sulfur chemical potential $\Delta\mu_{\mathrm{S}}$ is linked to sulfur fugacity through the equation:

$$\Delta\mu_{\mathrm{S}} = RT\ln fS_2 \qquad (6)$$

This is the peer-reviewed, final accepted version for American Mineralogist, published by the Mineralogical Society of America.
The published version is subject to change. Cite as Authors (Year) Title. American Mineralogist, in press.
DOI: https://doi.org/10.2138/am-2022-8207. http://www.minsocam.org/

where the $R$ and $fS_2$ denote gas constant and $S_2$ vapor fugacity, respectively.

The incorporation-energy-levels, $\varepsilon_i$, were calculated from the difference between the incorporation energies of any incorporation type and that of the ground state ($E_0$, the lowest incorporation energy).

$$\varepsilon_i = E_i - E_0. \qquad (7)$$

If ground state is estimated to be the substitution of Au for the Fe site, the incorporation-energy-levels of the Fe, S, and interstitial sites are $\varepsilon_0 = \varepsilon_{Fe} = 0$ eV, $\varepsilon_S$, and $\varepsilon_{int.}$, respectively. Combining Eqs. (1) and (2), one can get an equation set:

$$\begin{cases} p_S = P_{Fe} e^{-\frac{\varepsilon_S}{kT}} \\ p_{int.} = P_{Fe} e^{-\frac{\varepsilon_{int.}}{kT}} \\ p_S + P_{Fe} + p_{int.} = 1 \end{cases}, \qquad (8)$$

from which the occurrence probability of the substitution of Au for Fe ($p_{Fe}$), S ($p_S$), and the interstitial sites ($p_{int}$) can be derived. In a given condition of $\Delta\mu_S$ and $T$, the occurrence probabilities, $p_i$, can be calculated by resolving the equation set (8).

**Simulations of HAADF-STEM images and EELS spectra**

The fast simulation of high-angle annular dark field transmission electron microscope (HAADF-STEM) images was performed on a program based on kinematic-scattering method (He et al. 2015) using cluster models containing more than 1000 atoms along the [001] direction. We employed a Gaussian width (i.e., probe size of a real transmission electron microscope (TEM)) of 0.7 Å for simulations, because such a probe size can be easily reached in a modern TEM with spherical aberration corrector. The simulations of electron energy loss spectroscopy (EELS) were performed using the

Wien2K code (Blaha et al. 2020) with operation voltage at 200 kV. The input configurations for Wien2K calculations were relaxed from the VASP code. In Wien2K calculations, the PBE functional and a default $R_{MT}$ and $RK_{max}$ were employed, which were sufficient to reach the same convergence. A 0.5 eV of broaden width was employed for all the EELS spectra.

## Results

### Site occupation and valence of gold in pyrite

The structure of pyrite consists of [$FeS_6$] octahedra connected by S dimers through corner sharing (Fig. 1a). There are three possible pyrite sites for Au to reside in, i.e., the Fe, the S, and the interstitial sites (Figs. 1b-1d). The first two are sites where one Au can substitute for one Fe or S atom, while the third one requires extra space for Au to be incorporated into the host pyrite lattice. The Fe site has the first coordination shell composed of six S ions (Fig. 1b) while the coordination shell of S consists of three Fe and one S ions (Fig. 1c). In the cases that the interstitial sites are occupied by Au, the interstitial Au atoms are usually coordinated with four Fe and six S ions (Fig. 1d).

We constructed separate configurations for the above-mentioned triple-occupation models. The optimized structural properties show that incorporation of Au can increase the lattice size of pyrite from 159.31 to 159.93, 160.54, and 163.49 $Å^3$ per unit cell with Au incorporation in the Fe, S and interstitial sites, respectively. The increase in cell volume may lead to lattice strain, and thereby decrease the stability of the system (Han et al. 2019). Thus, pyrite with Au at the interstitial sites could be the most unstable of the three configurations, consistent with the estimated occurrence probability discussed below.

This is the peer-reviewed, final accepted version for American Mineralogist, published by the Mineralogical Society of America.
The published version is subject to change. Cite as Authors (Year) Title. American Mineralogist, in press.
DOI: https://doi.org/10.2138/am-2022-8207. http://www.minsocam.org/

We analyzed the valence state of Au in pyrite using the Bader charge (Bader 1990). The results show (Figs. 1b-1d) that gold can be negative (-0.09), positive (+0.30), and zero valence when it occupies the S, Fe, and interstitial sites, respectively. These results are consistent with reference materials with known valence state of Au, including CsAu (Au valence negative, Bader charge = -0.76), AuS (Au valence positive, Bader charge = +0.24), and metallic gold (Au valence 0, Bader charge = 0).

The structural stability of the Au-bearing pyrite was further evaluated via AIMD at room temperature (298 K). The analyses of AIMD trajectories show that the substitution models of Au-bearing pyrite are stable while the one with interstitial sites occupied by Au is unstable. The Au atoms are localized at either Fe or S sites during the 10 ps of AIMD. Meanwhile, the interstitial Au atom diffuses in the lattice and thereby exchanges with one Fe atom in pyrite in 4 ps of AIMD. Ultimately, the Au atom occupies the Fe site while the exchanged Fe atom relocates to the interstitial site (see details in supplementary video1).

We calculated the radial distribution functions (RDF) and coordination numbers (CN), using AIMD, to characterize local structures of Au-bearing pyrites. The results (Figs. 1e-1g) shows that Au incorporation can only influence the bond length as the CN of Au at the Fe and S sites remain the same with the substituted Fe and S ions. Since the interstitial model is unstable and readily evolves to the Fe substitution configuration, we only computed the RDF and CN for the substitution models after reaching equilibrium of the AIMD runs. When Au occupies the Fe or S sites in pyrite, the pair separation distances of the first coordination shell (i.e., the bond length) of Au-S are 2.46 and 2.26 Å, respectively, longer than those of Fe-S (2.26 Å) and S-S (2.16 Å) in pure pyrite. The increase in the bond length

(from Fe-S and S-S to Au-S) presumably is responsible for the increase in the lattice parameter as described above.

We also simulated measurable structural properties of gold-bearing pyrite. The occurrence of gold in the pyrite lattice sites (Figs. 2a-2c) can be readily visualized by simulated HAADF-STEM images. The intensity distribution of the HAADF-STEM image of pure pyrite (Fig. 2a) possesses a uniform nature with small variation induced by thermal fluctuation. The intensity distributions of HAADF-STEM images of gold-bearing pyrite (Figs. 2b-2c) show sharp peaks where a gold atom occurs. The peaks are symmetrical and asymmetrical when Au atoms locate at Fe and S sites, respectively. The intensity distributions of HAADF-STEM (profiles in Figs. 2a-2c) are proportional to $Z^n$ which describes the departure of scattering cross-section to the ideal Rutherford scattering, where $Z$ is the atomic number of atoms involved and $n$=2 is the power exponent (He et al. 2015).

Comparable to the three reference materials having various valence states of Au (Fig. 2e), the simulated Au $M_{4,5}$ EELS spectra of gold-bearing pyrites with Au located at various lattice sites (Fig. 2d) are distinguishable from each other. When Au substitutes for S in pyrite, three notable characteristic peaks occur in the Au $M_4$ EELS spectrum, similar to those of CsAu with gold in the -1 valence. The interstitial gold in pyrite possesses similar features of gold metal (one sharp with two shoulder peaks at the low energy side), suggesting the zero valence of the Au atom. However, the Au $M_4$ EELS spectrum of the gold-bearing pyrite with gold located at Fe sites is slightly different from that of AuS although the Bader charges of both materials are positive.

The presence of Au in the Fe and S sites in pyrite can also shift the vibrational property of the

This is the peer-reviewed, final accepted version for American Mineralogist, published by the Mineralogical Society of America.
The published version is subject to change. Cite as Authors (Year) Title. American Mineralogist, in press.
DOI: https://doi.org/10.2138/am-2022-8207. http://www.minsocam.org/

host mineral. The calculated vibrational spectra (Fig. 3), based on the AIMD trajectories, show that the spectra of gold substitutional pyrites shifted to lower wavenumber compared to that of pure pyrite, indicating that the incorporation of gold weakened the vibrations. When Au substitute for either Fe or S in pyrite, the vibrations at the wavenumber greater than 380 $cm^{-1}$ and smaller than 320 $cm^{-1}$ weakened, while those ranged from 320 to 380 $cm^{-1}$ strengthened, indicating that the substitution of Au into pyrite can vastly shift the lattice dynamics.

**Physicochemically controlled occurrence of gold in pyrite**

The calculated incorporation energy (Fig. 4) based on Eq. (3) shows that the ground state (i.e., $\varepsilon_0$, the lowest energy) of the incorporation-energy-levels varies at different ranges of sulfur chemical potential. The ground state was estimated to be the S sites when the sulfur chemical potential is less than -0.566 eV relative to the α-S crystal. In contrast, it changes into the Fe sites when the system possesses higher sulfur chemical potential (> -0.566 eV). Combining Eqs. (1)–(8), the occurrence probability of Au in pyrite is linked to sulfur fugacity. The results (Fig. 5) show that gold atoms mainly occupy either Fe or S sites under various physicochemical conditions. The sum of the occurrence probabilities of Au sitting at Fe and S sites under certain $fS_2$ and $T$ is very close to 1, while the highest occurrence probability of Au located at the interstitial sites is smaller than $10^{-49}$. Gold atoms prefer to occupy Fe sites under relatively high $fS_2$ and low $T$ while the preferred occupying shifts to S sites under inverse conditions.

## Discussion

This is the peer-reviewed, final accepted version for American Mineralogist, published by the Mineralogical Society of America.
The published version is subject to change. Cite as Authors (Year) Title. American Mineralogist, in press.
DOI: https://doi.org/10.2138/am-2022-8207. http://www.minsocam.org/

220 **Chemical speciation of "invisible" gold in pyrite.**

221 The results presented above may offer important clues through which the inconsistency in the
222 existing interpretations of Au speciation in pyritic structures can be readily understood. The most
223 widely accepted oxidation state of Au in pyritic structures is +1 from XANES results (Simon et al. 1999;
224 Merkulova et al. 2019). This may be caused by that most pyrite formed under sulfur-rich conditions,
225 and Au prefers to occupy the Fe sites in pyrite (Fig. 5). Recent results from HR-XANES show that Au
226 locates at Fe sites and the Au coordinates with 5.7 ± 0.7 S atoms at 2.41 Å (Merkulova et al. 2019),
227 consistent with our theoretical model for Au substitution of Fe in this study (Fig. 1f). The negative
228 valence of Au in both pyrite and arsenopyrite was first confirmed by XPS (Li et al. 1995) and further
229 supported by $^{197}$Au Mössbauer spectra (Li et al. 2002). This interpretation is consistent with our
230 theoretical model for Au substitution of S in this study (Fig. 1g), which confirms that the Au substituting
231 S in pyrite possesses negative valence.

232 **Implications for gold recovery and interpretation of formation conditions of ore deposits**

233 The relation between $fS_2$ and the occurrence probability of Au in the pyrite lattice (Fig. 5),
234 presented in this study, is consistent with previous experimental data showing that Au occupies the Fe
235 sites when the $\log fS_2$ varies from -3 to -1 bar under 450°C and 1 kbar (Trigub et al. 2017). This is
236 critical for gold recovery, as the recovery of refractory gold ore is mainly restrained by the occurrence of
237 gold in pyrite. Most of Au in refractory ore occurs as nanoparticles or lattice-bound form. Since the
238 lattice-bound form is stable under wide physicochemical conditions with active interstitial form (Fig. 5),
239 the interstitial Au could be considered as the initial form of Au nanoparticles formation when the gold

concentration surpasses its solubility in pyrite (Reich et al. 2005). Therefore, the recovery of the gold nanoparticles from pyrite may be implemented without destroying pyrite structure, while the recovery of lattice-bound gold involves the ruin (e.g., oxidation) of pyrite lattice.

The occurrence of Au in the pyrite lattice, experimentally measurable through either spectroscopy (such as XPS, XANES, in-situ EELS, and Mössbauer) or microscopy such as HAADF-STEM (Fig. 2), can be used to directly interpret the physicochemical conditions of ore deposits formation based on the relation shown in Fig. 5. Pyrite with dominant substitution of Au for Fe should be formed under lower $T$ and higher $fS_2$ in comparison to those with Au mainly occupying S sites. For instance, the refractory gold ore (in which gold occurs as +1 valence and occupies Fe sites) collected from a sandy mine tailing in Colombia, South America (Merkulova et al. 2019) may form under either relative lower $T$ or higher $fS_2$ than those (in which gold occurs as negative valence and occupies S sites) from Jinya gold deposits, Guangxi province, China (Li et al. 1995, 2002). Further, the correlation between Fe/S and Au concentrations in pyrite can also be used to indirectly substantiate the formation conditions of ore deposits as Au can occupy either Fe or S sites. From a Spearman rank correlation analysis (Xie et al. 2018), Au is found to negatively correlate with Fe, while no obvious correlation with S for Carlin-type ore pyrites from both Nevada, USA and Guizhou, China, suggesting that Au mainly occupies the Fe sites in pyrite. We thus infer that the Carlin-type gold deposits formed under relative low temperature and high $fS_2$. The stronger correlation of Au to Fe (-0.544) in Nevada deposits relative to that (-0.466) in Guizhou implies that the latter formed at higher $T$. This deduction is supported by previous experimental observations (S.CLlNE et al. 2013; Xie et al. 2018) that show the trapping

260 temperature of ore fluid in Guizhou is about 220° to 345°C, ~40° to 100°C higher than that in Nevada.

261

262 **Acknowledgements:** This work was supported by the National Key R & D Program of China
263 (2018YFA0702600), the China National Funds for Distinguished Young Scientists (41825003), the
264 National Natural Science Foundation of China (41921003), the Natural Science Foundation of
265 Guangdong Province, China (2019A1515011303), the Youth Innovation Promotion Association CAS
266 (2021353), and the Science and Technology Planning of Guangdong Province, China
267 (2020B1212060055).

268

269 **References**

270 Bader, R.F. (1990) Atoms in molecules. Wiley Online Library.

271 Benbattouche, N., Saunders, G.A., Lambson, E.F., and Honle, W. (1989) The dependences of the elastic
272 stiffness moduli and the Poisson ratio of natural iron pyrites $FeS_2$ upon pressure and temperature.
273 Journal of Physics D: Applied Physics, 22, 670–675.

274 Blaha, P., Schwarz, K., Tran, F., Laskowski, R., Madsen, G.K.H., and Marks, L.D. (2020) WIEN2k: An
275 APW+lo program for calculating the properties of solids. The Journal of Chemical Physics, 152,
276 074101.

277 Cabri, L.J., Newville, M., Gordon, R.A., Crozier, E.D., Sutton, S.R., McMahon, G., and Jiang, D.T.
278 (2000) Chemical speciation of gold in arsenopyrite. Canadian Mineralogist, 38, 1265–1281.

279 Chouinard, A., Paquette, J., and Williams-Jones, A.E. (2005) Crystallographic controls on trace-element
280 incorporation in auriferous pyrite from the Pascua Epithermal High-Sulfidation deposit, Chile–
281 Argentina. The Canadian Mineralogist, 43, 951–963.

282 Du, S., Wen, H., Liu, S., Qin, C., Yan, Y., Yang, G., and Feng, P. (2020) Mineralogy and metallogenesis
283 of the Sanbao Mn–Ag (Zn-Pb) deposit in the Laojunshan ore district, SE Yunnan province,
284 China. Minerals, 10, 650.

285 Dudarev, S.L., Botton, G.A., Savrasov, S.Y., Humphreys, C.J., and Sutton, A.P. (1998)

Electron-energy-loss spectra and the structural stability of nickel oxide: An LSDA+U study. Physical Review B, 57, 1505–1509.

Gulley, A.L., Nassar, N.T., and Xun, S. (2018) China, the United States, and competition for resources that enable emerging technologies. Proceedings of the National Academy of Sciences, 115, 4111–4115.

Han, H., Park, J., Nam, S.Y., Kim, K.J., Choi, G.M., Parkin, S.S.P., Jang, H.M., and Irvine, J.T.S. (2019) Lattice strain-enhanced exsolution of nanoparticles in thin films. Nature Communications, 10, 1471.

He, D.S., Li, Z.Y., and Yuan, J. (2015) Kinematic HAADF-STEM image simulation of small nanoparticles. Micron, 74, 47–53.

Henkelman, G., Arnaldsson, A., and Jonsson, H. (2006) A fast and robust algorithm for Bader decomposition of charge density. Computational Materials Science, 36, 354–360.

Humphrey, W., Dalke, A., and Schulten, K. (1996) VMD: visual molecular dynamics. Journal of Molecular Graphics, 14, 33–38, 27–28.

Jain, A., Ong, S.P., Hautier, G., Chen, W., Richards, W.D., Dacek, S., Cholia, S., Gunter, D., Skinner, D., Ceder, G., and others (2013) Commentary: The Materials Project: A materials genome approach to accelerating materials innovation. APL Materials, 1, 011002.

Kresse, G., and Furthmuller, J. (1996) Efficiency of ab-initio total energy calculations for metals and semiconductors using a plane-wave basis set. Computational Materials Science, 6, 15–50.

Kresse, G., and Joubert, D. (1999) From ultrasoft pseudopotentials to the projector augmented-wave method. Physical Review B, 59, 1758–1775.

Li, J., Feng, D., Qi, F., and Zhang, G. (1995) The existence of the negative charge of gold in sulphide minerals and its formation mechanism. Acta Geologica Sinica, 69, 67–77.

Li, J., Qi, F., Qingsheng, X., and Li, Z. (2002) Ascertainment of chemically bound gold and its valence state in arsenopyrite and arsenian pyrite from Jinya mine, Guangxi, China. Mineral Deposits, 21, 1160–1163.

Martyna, G.J., Klein, M.L., and Tuckerman, M. (1992) Nosé–Hoover chains: The canonical ensemble via continuous dynamics. The Journal of Chemical Physics, 97, 2635–2643.

Merkulova, M., Mathon, O., Glatzel, P., Rovezzi, M., Batanova, V., Marion, P., Boiron, M.-C., and Manceau, A. (2019) Revealing the chemical form of “invisible” gold in natural arsenian pyrite and arsenopyrite with high energy-resolution X-ray absorption spectroscopy. ACS Earth and

317 Space Chemistry, 3, 1905–1914.

318 Perdew, J.P., Burke, K., and Ernzerhof, M. (1996) Generalized gradient approximation made simple.
319 Physical Review Letters, 77, 3865–3868.

320 Pokrovski, G.S., Kokh, M.A., Proux, O., Hazemann, J.-L., Bazarkina, E.F., Testemale, D., Escoda, C.,
321 Boiron, M.-C., Blanchard, M., Aigouy, T., and others (2019) The nature and partitioning of
322 invisible gold in the pyrite-fluid system. Ore Geology Reviews, 109, 545–563.

323 Reich, M., Kesler, S.E., Utsunomiya, S., Palenik, C.S., Chryssoulis, S.L., and Ewing, R.C. (2005)
324 Solubility of gold in arsenian pyrite. Geochimica et Cosmochimica Acta, 69, 2781–2796.

325 Rettig, S.J., and Trotter, J. (1987) Refinement of the structure of orthorhombic sulfur, α-S8. Acta
326 Crystallographica Section C, 43, 2260–2262.

327 S.Cline, J., L.Muntean, J., Gu, X., and Xia, Y. (2013) A comparison of Carlin-type gold feposits:
328 Guizhou province, golden triangle, southwest China, and northern Nevada, USA. Earth Science
329 Frontiers, 20, 1–18.

330 Simon, G., Huang, H., Penner-Hahn, J.E., Kesler, S.E., and Kao, L.S. (1999) Oxidation state of gold and
331 arsenic in gold-bearing arsenian pyrite. American Mineralogist, 84, 1071–1079.

332 Suh, I.-K., Ohta, H., and Waseda, Y. (1988) High-temperature thermal expansion of six metallic
333 elements measured by dilatation method and X-ray diffraction. Journal of Materials Science, 23,
334 757–760.

335 Tang, W., Sanville, E., and Henkelman, G. (2009) A grid-based Bader analysis algorithm without lattice
336 bias. Journal of Physics: Condensed Matter, 21, 084204.

337 Trigub, A.L., Tagirov, B.R., Kvashnina, K.O., Chareev, D.A., Nickolsky, M.S., Shiryaev, A.A.,
338 Baranova, N.N., Kovalchuk, E.V., and Mokhov, A.V. (2017) X-ray spectroscopy study of the
339 chemical state of “invisible” Au in synthetic minerals in the Fe-As-S system. American
340 Mineralogist, 102, 1057–1065.

341 Wang, M., Xiang, X., Zhang, L., and Xiao, L. (2008) Effect of vanadium occurrence state on the choice
342 of extracting vanadium technology from stone coal. Rare Metals, 27, 112–115.

343 Wang, V., Xu, N., Liu, J.-C., Tang, G., and Geng, W.-T. (2021) VASPKIT: A user-friendly interface
344 facilitating high-throughput computing and analysis using VASP code. Computer Physics
345 Communications, 108033.

346 Wilburn, D.R., and Bassett, W.A. (1978) Hydrostatic compression of iron and related compounds; an
347 overview. American Mineralogist, 63, 591–596.

Xian, H., He, H., Zhu, J., Du, R., Wu, X., Tang, H., Tan, W., Liang, X., Zhu, R., and Henry Teng, H. (2019a) Crystal habit-directed gold deposition on pyrite: Surface chemical interpretation of the pyrite morphology indicative of gold enrichment. Geochimica et Cosmochimica Acta, 264, 191–204.

Xian, H., Zhu, J., Tan, W., Tang, H., Liu, P., Zhu, R., Liang, X., Wei, J., He, H., and Teng, H.H. (2019b) The mechanism of defect induced hydroxylation on pyrite surfaces and implications for hydroxyl radical generation in prebiotic chemistry. Geochimica Et Cosmochimica Acta, 244, 163–172.

Xian, H., Wu, X., Zhu, J., Du, R., Wei, J., Zhu, R., and He, H. (2021) Environmental-sulfur-controlled surface properties of pyrite: a first principles PBE + U study. Physics and Chemistry of Minerals, 48, 20.

Xie, Z., Xia, Y., Cline, J.S., Koenig, A., Wei, D., Tan, Q., and Wang, Z. (2018) Are there Carlin-type gold deposits in China? A comparison of the Guizhou, China, deposits with Nevada, USA, deposits. In J.L. Muntean, Ed., Diversity in Carlin-Style Gold Deposits Vol. 20, p. 0. Society of Economic Geologists.

Xing, Y., Brugger, J., Tomkins, A., and Shvarov, Y. (2019) Arsenic evolution as a tool for understanding formation of pyritic gold ores. Geology, 47, 335–338.

Zhai, M.-G., Wu, F.-Y., Hui, R.-Z., Jiang, S.-Y., Li, W., Wang, R., Wang, D.-H., Qi, T., Qin, K., and Wen, H.-J. (2019) Critical metal mineral resources: current research status and scientific issues. Bulletin of National Natural Science Foundation of China, 33, 106–111.

Zhang, Y.N., Hu, J., Law, M., and Wu, R.Q. (2012) Effect of surface stoichiometry on the band gap of the pyrite $FeS_2$(100) surface. Physical Review B, 85, 085314.

371 **Figure captions**

372 **Figure 1.** Structural models and partial radial distribution function (RDF, g($r$)) of gold-bearing pyrite.
373 A-D: Structural models of bulk pyrite (**a**), Au substitution of Fe (**b**) and S (**c**) sites, and Au occupation at
374 interstitial site (**d**) of pyrite; the yellow, brown, and orange spheres denote sulfur, iron, and gold atoms,
375 respectively. (**e**)–(**g**): Partial RDF of pure pyrite (**e**) and substitutional (**f** and **g**) Au-bearing pyrite.

376 **Figure 2.** Predicted structural properties of gold-bearing pyrite. (**a**)–(**c**) denote the atomic images of
377 HAADF-STEM for pure pyrite and pyrite with Au occupation at Fe and S sites, respectively. The scale
378 bars in (**a**)–(**c**) represent 5 nm. (**d**) and (**e**) denote EELS spectra of Au $M_{4,5}$ edge in gold-bearing pyrite
379 and reference materials, respectively.

380 **Figure 3.** Vibrational density of state of substitutional gold-bearing pyrite and pure pyrite.

381 **Figure 4.** Incorporation energy variation versus sulfur chemical potential change ($\Delta\mu_S$) of gold-bearing
382 pyrite.

383 **Figure 5.** Sulfur fugacity and temperature dependent occurrence probability of gold in pyrite. (**a**)–(**c**)
384 denote the Au occupation at Fe, S and interstitial sites in pyrite, respectively. The dash lines denote the
385 contour line of sulfur fugacity ($fS_2$) and the numbers on the dash lines are the corresponding log $fS_2$ in
386 bar. The color bars denote the occurrence probability of gold in the corresponding site.

387

This is the peer-reviewed, final accepted version for American Mineralogist, published by the Mineralogical Society of America.
The published version is subject to change. Cite as Authors (Year) Title. American Mineralogist, in press.
DOI: https://doi.org/10.2138/am-2022-8207. http://www.minsocam.org/

388 Figure 1

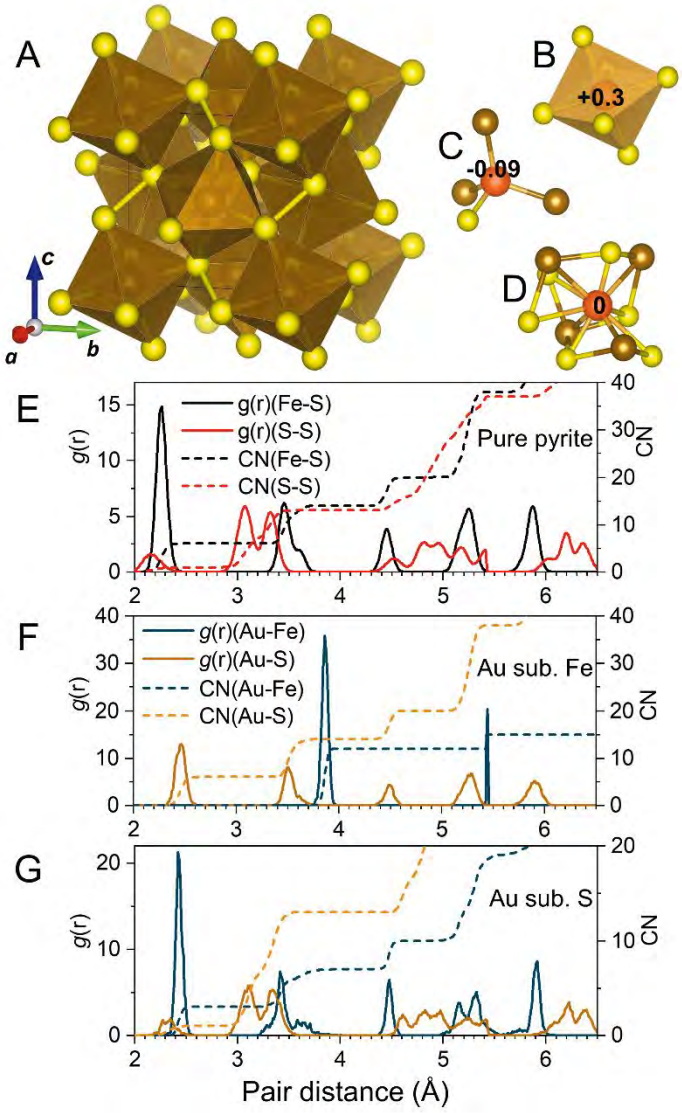


389

390

This is the peer-reviewed, final accepted version for American Mineralogist, published by the Mineralogical Society of America.
The published version is subject to change. Cite as Authors (Year) Title. American Mineralogist, in press.
DOI: https://doi.org/10.2138/am-2022-8207. http://www.minsocam.org/

391 Figure 2

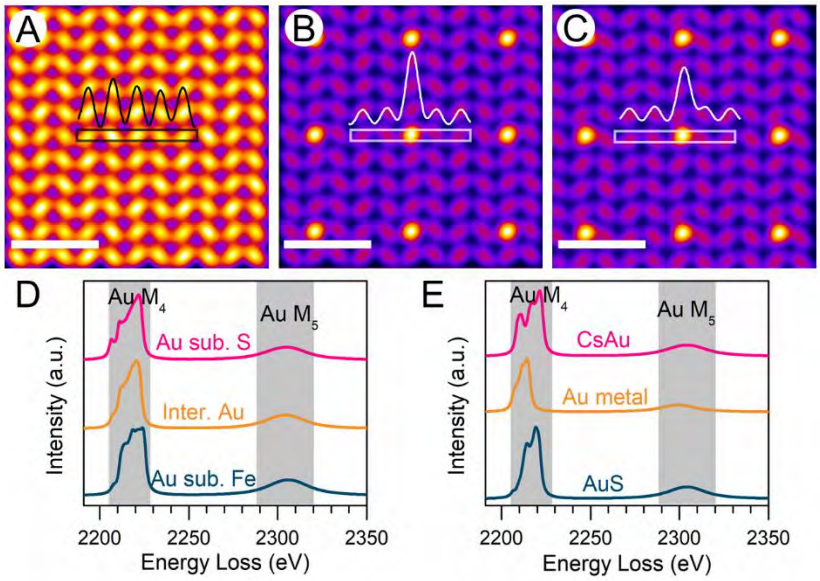


392

393

This is the peer-reviewed, final accepted version for American Mineralogist, published by the Mineralogical Society of America.
The published version is subject to change. Cite as Authors (Year) Title. American Mineralogist, in press.
DOI: https://doi.org/10.2138/am-2022-8207. http://www.minsocam.org/

394 Figure 3

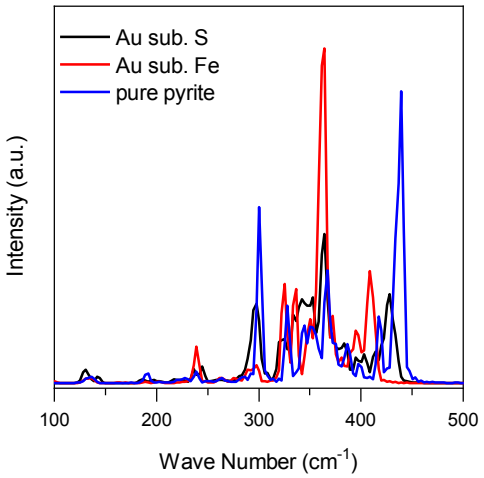


395

396

397

398 Figure 4

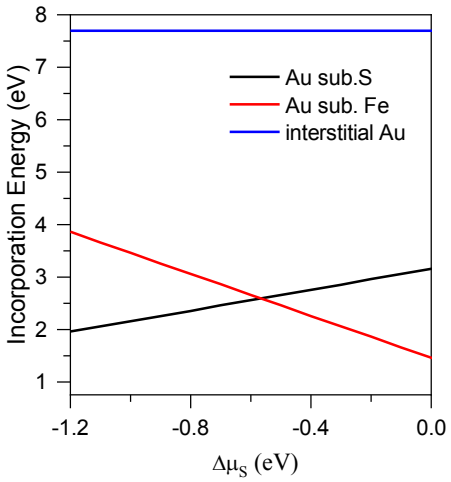


399

400

This is the peer-reviewed, final accepted version for American Mineralogist, published by the Mineralogical Society of America.
The published version is subject to change. Cite as Authors (Year) Title. American Mineralogist, in press.
DOI: https://doi.org/10.2138/am-2022-8207. http://www.minsocam.org/

401 Figure 5

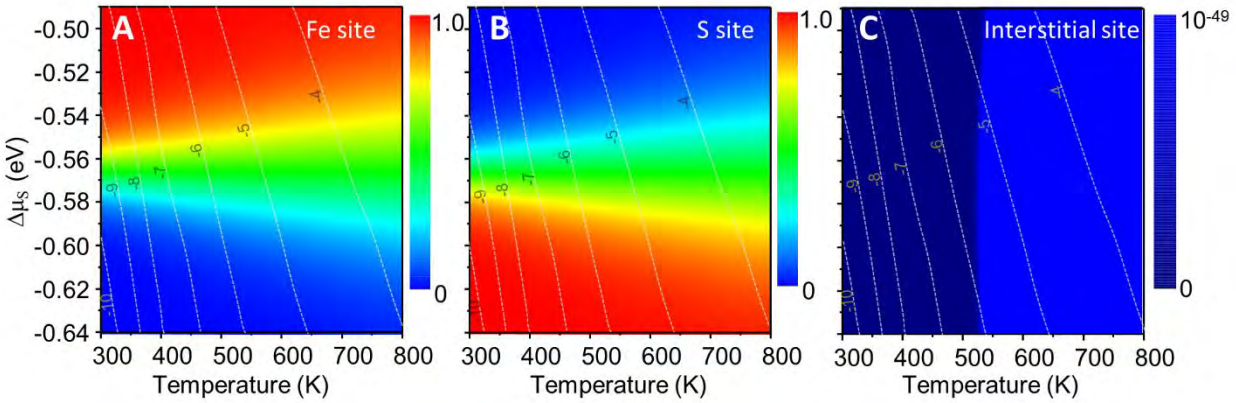


402

403

This is the peer-reviewed, final accepted version for American Mineralogist, published by the Mineralogical Society of America.
The published version is subject to change. Cite as Authors (Year) Title. American Mineralogist, in press.
DOI: https://doi.org/10.2138/am-2022-8207. http://www.minsocam.org/

404 **Table 1.** Comparison of calculated and experimental lattice parameters for minerals and structures
405 employed in this study.

| Mineral and structures | Lattice parameters | | Data source |
|---|---|---|---|
| | *a, b, c* /Å | *α, β, γ* /° | |
| Experimental pyrite | 5.418, 5.418, 5.418 | 90, 90, 90 | Benbattouche et al. (1989) |
| Theoretical pyrite | 5.423, 5.423, 5.423 | 90, 90, 90 | This study |
| Theoretical pyrite with Au sub. Fe | 10.8880, 10.8880, 10.8880 | 90, 90, 90 | This study |
| Theoretical pyrite with Au sub. S | 10.8701, 10.8701, 10.8701 | 90, 90, 90 | This study |
| Theoretical pyrite with interstitial Au | 10.9012, 10.9326, 10.9732 | 90.1, 90.3, 90.1 | This study |
| Experimental metallic gold | 4.072, 4.072, 4.072 | 90, 90, 90 | Suh et al. (1988) |
| Theoretical metallic gold | 4.0783, 4.0783, 4.0783 | 90, 90, 90 | This study |
| Experimental metallic iron | 2.866, 2.866, 2.866 | 90, 90, 90 | Wilburn & Bassett (1978) |
| Theoretical metallic iron | 2.8664, 2.8664, 2.8664 | 90, 90, 90 | This study |
| Experimental alpha-S8 | 10.4646, 12.8660, 24.4860 | 90, 90, 90 | Rettig & Trotter (1987) |
| Theoretical alpha-S8 | 10.4646, 12.8660, 24.4860 | 90, 90, 90 | This study |
| Referred theoretical AuS | 3.9331, 3.9331, 6.8182 | 90, 90, 120 | Material Project-984598_AuS |
| Theoretical AuS | 3.8972, 3.8972, 6.8257 | 90, 90, 120 | This study |
| Referred theoretical CsAu | 4.3811, 4.3811, 4.3811 | 90, 90, 90 | Material Project-2667_CsAu |
| Theoretical CsAu | 4.3811, 4.3811, 4.3811 | 90, 90, 90 | This study |